

Magnetization of the Martian crust

Jafar Arkani-Hamed

Earth and Planetary Sciences, McGill University, Montreal, Quebec, Canada

Received 29 March 2001; revised 27 July 2001; accepted 10 October 2001; published 28 May 2002.

[1] This paper presents the lateral variations of the vertically averaged magnetization model of the Martian crust determined from the degree 50 spherical harmonic model of the magnetic potential. The model potential is derived using the Mars Global Surveyor low-altitude magnetic data acquired within elevations of 85–200 km. The potential model is first verified by comparing the three orthogonal components of the corresponding vector field with the observed high-altitude (~ 380 km) data. Using the paleopole positions calculated through modeling 10 isolated, small magnetic anomalies, the model potential is inverted to determine the vertically averaged magnetization of a nominal 50 km thick crust. The crust is highly magnetic, with a magnetization contrast (peak-to-trough) as high as 35 A/m. The lack of distinct magnetic signatures for the giant impact basins, Hellas, Argyre and Isidis, and the absence of a magnetic anomaly associated with the north-south topographic dichotomy indicate that the upper parts of the crust are low magnetic and that the strong magnetic source bodies are in the lower parts. *INDEX TERMS:* 6225

Planetology: Solar System Objects: Mars; 5430 Planetology: Solid Surface Planets: Interiors (8147); 5475 Planetology: Solid Surface Planets: Tectonics (8149); 5499 Planetology: Solid Surface Planets: General or miscellaneous; *KEYWORDS:* Mars magnetism, crustal magnetization of Mars, paleomagnetic poles of Mars, magnetic anomalies of Mars

1. Introduction

[2] The magnetic map of Mars derived by *Acuna et al.* [1999] from the low-altitude Mars Global Surveyor data that were acquired within 85–200 km altitudes shows strong anomalies over Terra Cimmeria and Terra Sirenum and no comparable anomalies in the northern hemisphere as well as over $\sim 1/3$ of the southern hemisphere. The anomalies were presented without altitude corrections. *Purucker et al.* [2000] reduced the radial component anomalies to a constant elevation of 200 km. The resulting map was much smoother and confirmed the major features seen on *Acuna et al.*'s map. *Arkani-Hamed* [2001a] derived a 50 degree spherical harmonic model of the magnetic potential at 120 km altitude using three orthogonal components of the magnetic field data, and *Ferguson et al.* [2000] presented a 70 degree model. The second section of this paper verifies the degree 50 model potential by comparing the three components of the magnetic field determined from the model with those derived from the recently available high-altitude magnetic data. Also, the degree 50 model is compared with the degree 70 model of *Ferguson et al.*, and the radial component of the degree 50 model is compared with the radial component map produced by *Purucker et al.*

[3] The strong magnetic anomalies of Terra Cimmeria and Terra Sirenum arise from large and closely placed complex magnetic bodies. It is impossible to determine the direction of magnetization of these bodies directly from their magnetic anomalies, largely because of strong overlapping of the magnetic fields of adjacent bodies. For example, *Purucker et al.* [2000] used an array of vertical dipoles on Mars to model the observed anomalies. An array of nonvertical dipoles with different distribution and intensities can also give rise to the same anomalies. The substantial overlapping of these strong anomalies precludes the determination of the paleomagnetic pole position of Mars on the basis of these anomalies. However, there are a few small, well-isolated, and almost circular anomalies that can be modeled by simple bodies

of uniform magnetization. The direction of magnetization of these isolated bodies should reflect the orientation of the paleomagnetic field [*Arkani-Hamed*, 2001b]. The third section presents the paleomagnetic pole positions determined by modeling 10 such isolated anomalies in terms of vertical prisms of elliptical cross sections, assuming that an individual body is magnetized along a dipole core field. A more representative pole position (25°N , 230°E) is used in the next section to determine a global magnetization map of the crust. The final section addresses two general scenarios for the magnetization of the crust and includes concluding remarks.

2. Verifying the Degree 50 Model Potential

[4] The low-altitude magnetic data have a global coverage, but with many gaps parallel to the satellite tracks. They span a 85–200 km altitude range which is comparable to the mean elevation of the spacecraft, and simple vertical averaging of the data is inadequate. *Purucker et al.* [2000] used a vertical dipole array at the surface of Mars as an equivalent source and reduced the radial component data to a two-dimensional (2-D) map at a constant altitude of 200 km, the upper limit of the altitude range of the data. To better retain the short wavelength components of the magnetic anomalies, *Arkani-Hamed* [2001a] derived a 50 degree spherical harmonic model of the magnetic potential field at 120 km altitude (Figure 1), which is in the middle of the altitude range of the data, using all three components of the magnetic field. The model has a wavelength resolution of ~ 425 km, with the wavelength-to-altitude ratio of ~ 3.6 for the shortest wavelength retained. The resolution is limited largely because of data gaps mentioned. The recently available high-altitude data provide a good opportunity to verify the degree 50 model potential, before making any attempt to interpret the anomalies. The small altitude variations of Mars Global Surveyor during the high-altitude data acquisition (± 30 km) relative to its mean elevation of ~ 380 km (i.e., $<8\%$ of the mean elevation and $<7\%$ of the shortest wavelength of the degree 50 model potential) allow vertical stacking of the data without substantially perturbing major anomalies. Therefore I

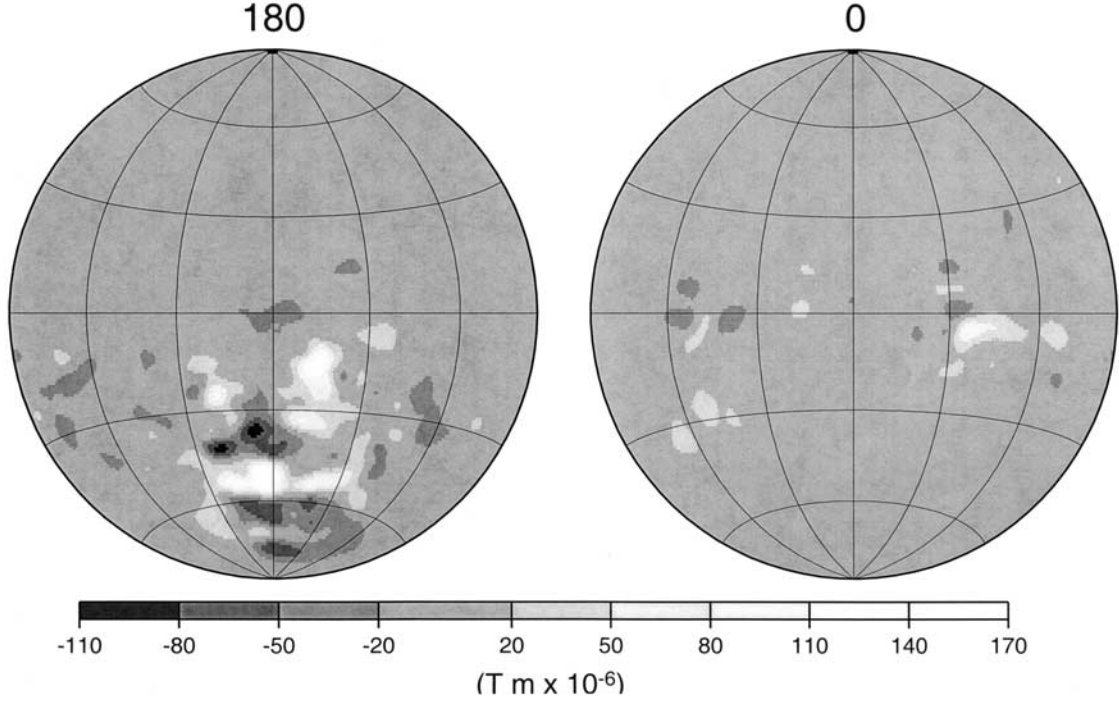


Figure 1. The degree 50 spherical harmonic model of Mars' magnetic potential at 120 km altitude.

averaged each component of the nighttime high-altitude data within a given bin of 1×1 degree, after removing some outliers that were farther than two standard deviations from the mean value of the bin. Although the satellite tracks densely covered the region, there were some thin gaps parallel to the tracks. These data gaps were filled by a 2-D weighted interpolation filter, using the 2-D Hanning function as a weighting factor,

$$W = 0.5[1 + \cos(\pi x/R)], \quad (1)$$

where x is the distance from a grid point to be filled and R ($= 120$ km) is the radius of the filter. The resulting maps were then smoothed using a weighted averaging by a similar filter but with the R value of 180 km. The smoothed maps are regarded suitable for comparison purposes only.

[5] Figure 2 shows the radial and the west-east component maps derived from the high-altitude data and those calculated by upward continuation of the 50 degree model potential to 380 km elevation. I used the high-altitude data that were available in the fall of 2000. No data were available for latitudes higher than $\sim 60^\circ\text{N}$. However, the data have covered almost all of the magnetic anomalies of Mars. The radial component is least disturbed by noncrustal sources, whereas the west-east component may have contributions from ionospheric currents and is the most disturbed compared to the other components [Acuna *et al.*, 1999]. The anomalies seen in the corresponding maps are very similar, which is also the case for the north-south component maps not shown here. The amplitudes of the high-altitude data maps are slightly smaller than those of the degree 50 model potential, possibly owing to vertical averaging and subsequent filling of the gaps and applying the smoothing filter. This close similarity of the anomalies emphasizes that the ionospheric contributions are small (see section 5) and possibly similar at both elevations and that the anomalies are largely of crustal origin. The well-defined and almost equidimensional strong anomalies seen in the west-east component maps over Terra Cimmeria, where the radial component maps show west-east trends, do not support a seafloor spreading type model for the crustal magnetization (see below). The degree 50 model potential

will be used in the rest of this paper partly because it is derived from data with a global coverage and partly because it is derived from the low-altitude data, where the possible external field contribution is negligible compared to the crustal one.

[6] The degree 50 model is also compared with the degree 70 model derived by *Ferguson et al.* [2000], who used completely different procedures and not an identical data set. Figure 3a shows the power spectra R_n of the two models determined by

$$R_n = (n+1) \sum_{m=0}^n [g_{nm}^2 + h_{nm}^2], \quad (2)$$

where g_{nm} and h_{nm} denote the spherical harmonic coefficients of a given model. The two models have almost identical power, except for harmonics of degree < 4 . The similarity of the models is also illustrated by their degree correlation coefficients η_n (Figure 3b), calculated from

$$\eta_n = \frac{\sum_{m=0}^n (g_{nm}g'_{nm} + h_{nm}h'_{nm})}{[\sum_{m=0}^n (g_{nm}^2 + h_{nm}^2) \times \sum_{m=0}^n (g'_{nm}^2 + h'_{nm}^2)]^{1/2}}, \quad (3)$$

where the primed coefficients are for one of the models and the unprimed ones for the other. The two models correlate very well with correlation coefficients higher than 0.9 and mainly higher than 0.95, except for harmonics of degree 2 with a correlation coefficient of 0.81, which is still very high. These long-wavelength harmonics have minor contributions to the localized magnetic anomalies. Also included in Figure 3b are the degree correlation coefficients of the radial component of the degree 50 model with the radial component map derived by *Purucker et al.* [2000]. Although the degree 50 model correlates less with Purucker *et al.*'s map than with Ferguson *et al.*'s model, the correlation coefficients are still very high, higher than 0.8 almost over the entire spectrum.

[7] The very high correlation and almost identical power spectra of the degree 50 model potential and the degree 70 potential model of *Ferguson et al.* [2000], the good correlation of the radial

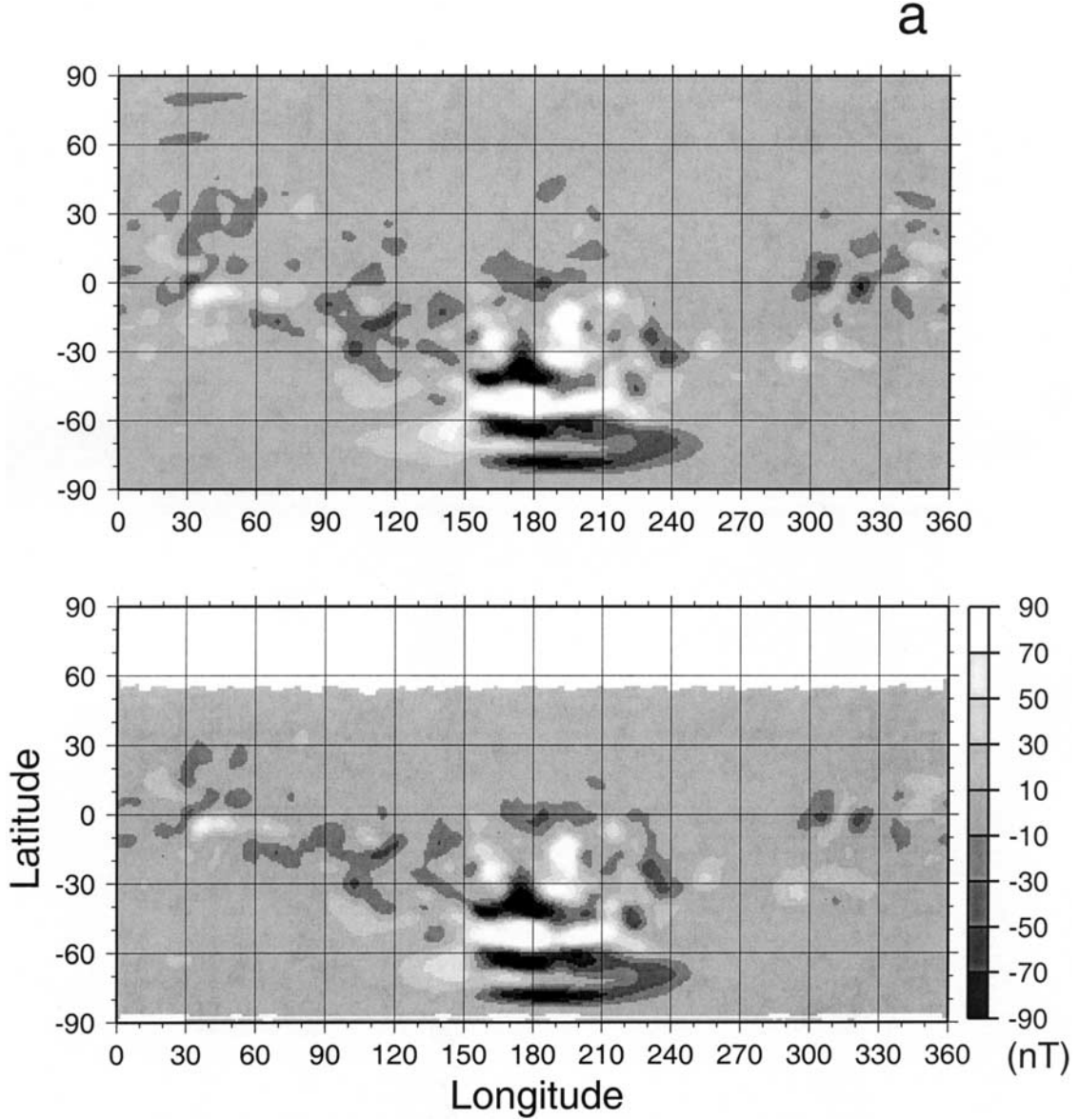


Figure 2. (a) (top) The radial component of magnetic field at 380 km altitude from the upward continued degree 50 model potential and (bottom) the high-altitude data. (b) (top) The west to east component of the magnetic field at 380 km altitude from the upward continued degree 50 model potential and (bottom) the high-altitude data.

component of the degree 50 model with that of *Purucker et al.* [2000], and the strong similarity of the three orthogonal components of the magnetic field derived from the degree 50 model with those measured at high altitudes indicate that the degree 50 model potential is quite reliable over its entire spectrum. The degree 50 model is used in the following to determine the paleomagnetic pole positions and the lateral variations of the vertically averaged magnetization of the Martian crust.

3. Paleomagnetic Poles of Mars

[8] Determination of the crustal magnetization from the magnetic anomaly data is inherently nonunique. The lack of core field at present provides no clue about the direction of the core field some 4 Gyr ago. This introduces an extra nonuniqueness to the crustal magnetization. The large magnetic anomalies over Terra Cimmeria and Terra Sirenum do not provide any viable information about the direction of the core field that magnetized the source bodies, partly because of strong overlapping of the magnetic field

of neighboring sources and partly because of possibly appreciable variations of the magnetization inside the large magnetic bodies. On the other hand, small and well-isolated anomalies with simple shapes can be safely modeled in terms of uniformly magnetized simple bodies. The anomalies must be large enough to be fully resolved by the data and isolated enough to avoid overlapping their magnetic signatures with those of other sources. *Hood and Zakharian* [2001] modeled two isolated anomalies in the northern hemisphere in terms of single dipoles and circular disks and determined the locations of the paleomagnetic poles of Mars. In this section I model 10 small and isolated anomalies in terms of vertical prisms of elliptical cross sections using a Fourier domain algorithm. Elliptical prisms are employed because by varying the semimajor and semiminor axes and the orientation of the elliptical cross section it is possible to better model a given magnetic anomaly. Preliminary modeling using prisms with circular and elliptical cross sections showed that the direction of magnetization is sensitive to the shape of the prism, although the intensity of magnetization is not as much. The sizes of the anomalies are larger

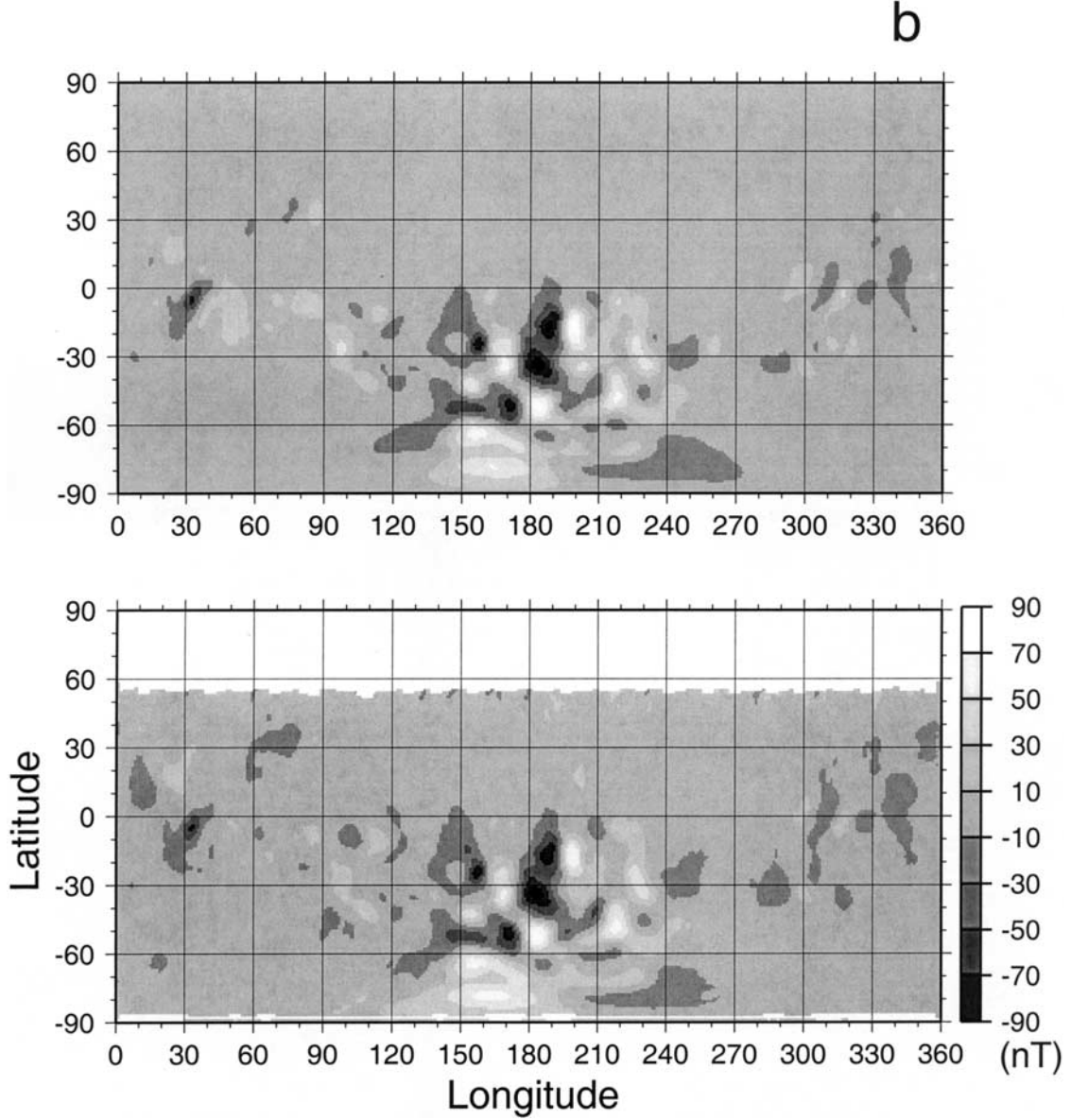


Figure 2. (continued)

than the resolution limit of the degree 50 model potential. They have similar shapes and magnitudes in the upward continued degree 50 model and high-altitude maps (Figure 2).

3.1. Prism Models

[9] The magnetic potential V^p of a uniformly magnetized vertical prism of an elliptical cross section is

$$V^p(x, y, z) = \int \int \int \mathbf{M}_0(\mathbf{x}_0, \mathbf{y}_0, \mathbf{z}_0) \cdot \nabla_o \frac{1}{|\mathbf{r} - \mathbf{r}_0|} dx_o dy_o dz_o, \quad (4)$$

where x, y , and z are the rectangular coordinates of the observation point \mathbf{r} ; x_o, y_o , and z_o are those of the source point \mathbf{r}_0 ; \mathbf{M}_0 is the uniform magnetization of the prism; and ∇_o is the gradient operator in the \mathbf{r}_0 domain. The integration is over the entire prism. Taking a 2-D Fourier transform of this equation yields

$$\mathbf{V}^p(\xi, \eta, z) = -\frac{2\pi}{K^2} e^{-Kz} (1 - e^{-KH}) (\vec{\gamma} \cdot \mathbf{M}_0) \mathbf{S}(\xi, \eta), \quad (5)$$

where

$$\vec{\gamma} = (i\xi, i\eta, -K); \quad K = (\xi^2 + \eta^2)^{1/2}. \quad (6)$$

\mathbf{V}^p is the 2-D Fourier transform of the magnetic potential; ξ and η are wave numbers in the x (east) and y (north) directions; H is the depth to the bottom of the prism, assumed to be 10 km with the top of the prism at the surface; z (positive upward) is the altitude of observation, 120 km; and \mathbf{S} is the 2-D Fourier transform of the elliptical shape of the prism cross section. The cross section has a semimajor axis \mathbf{a} and a semiminor axis \mathbf{b} . Its semimajor axis is oriented at an angle Ω with respect to the west-east line. The Fourier domain calculation is much more efficient than a space domain calculation, especially for nonaxisymmetric elliptical prisms. Magnetic anomaly analysis provides the lateral variations of the bulk magnetization (the vertically integrated magnetization) of the source body regardless of the method of analysis. Increasing the prism thickness requires decreasing the magnetization and vice versa but has no effect on the direction of

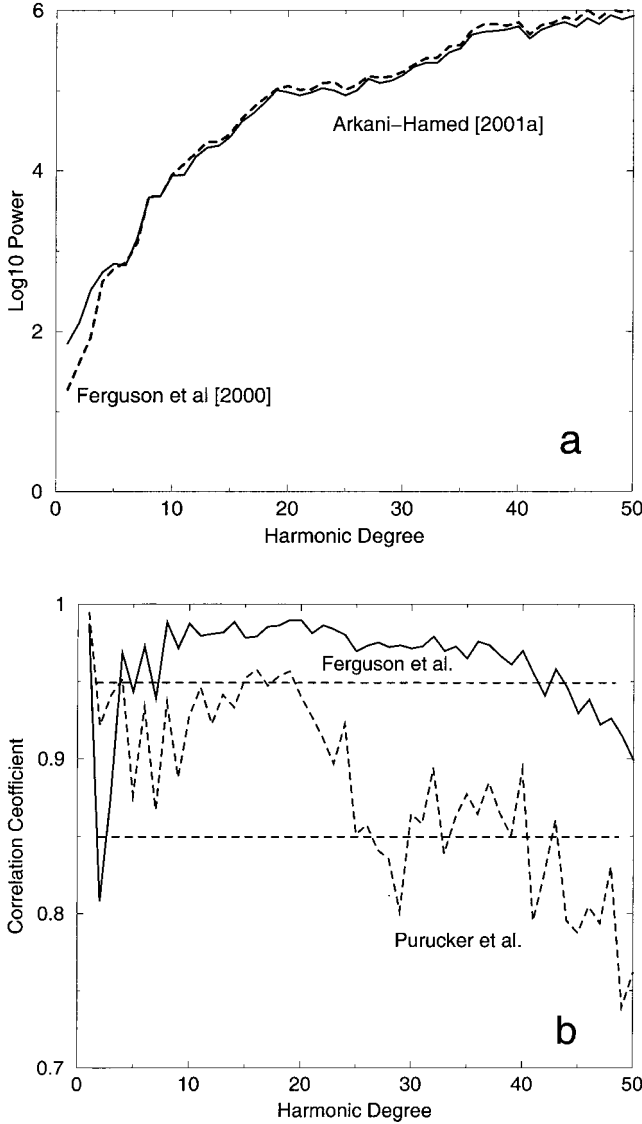


Figure 3. (a) The power spectra of the degree 50 model potential of *Arkani-Hamed* [2001a] and that of *Ferguson et al.* [2000]. (b) The degree correlation of the model potentials of *Arkani-Hamed* [2001a] and *Ferguson et al.* [2000] and the degree correlation of the radial magnetic field component of the degree 50 model with that of *Purucker et al.* [2000].

magnetization determined in this section. Also, the placement of the top of the prism at the surface, rather than at a certain plausible depth, has minor effects on the magnetic field calculated at 120 km altitude.

[10] An isolated magnetic potential anomaly, extracted from the degree 50 spherical harmonic model at a 120 km elevation, is mapped on a 2-D equal distance 128×128 grid of 15 km intervals. The dimension of the map is 3–4 times larger than that of the source body (see below). The center of the source body was visually depicted using six maps: north, east, and vertical component maps derived from the upward continued degree 50 model and those from the high-altitude data. A two-dimensional circular filter, cocentered with the source body, is applied to the magnetic potential anomaly in order to minimize the magnetic field of nearby sources. The filter sets to zero the anomalies outside a radial distance R , leaves unchanged those inside a radial distance R' , and gradually tapers the data between R' and R by a Hanning

function. The optimum R and R' values for each anomaly were determined through systematic application of the filter using different values for these parameters. The finally selected R and R' values are 400–500 km and 300–350 km, respectively, depending on the size of the anomalies. The magnetization vector of a prism is calculated by least squares fitting its magnetic potential, which was also circularly filtered, to the filtered 50 degree potential anomaly as follows.

[11] Let V^x , V^y , and V^z denote the circularly filtered magnetic potentials of a prism that is magnetized in the x , y , and z directions, respectively, with a magnetization of 1 A/m, and V^o be the circularly filtered observed potential anomaly. The x , y , and z components of the magnetization vector (M_o^x , M_o^y and M_o^z) are determined by minimizing

$$\epsilon^2 = \sum_{ij} \left[V_{ij}^o - \left(M_o^x V_{ij}^x + M_o^y V_{ij}^y + M_o^z V_{ij}^z \right) \right]^2, \quad (7)$$

where the indices i and j denote the i , j th grid node. To obtain the best fitted model, the prism parameters are varied: **a** is incrementally increased from 75 to 450 km at a 15 km increment, **b** is changed from **a**/2 to **a** with an increment of 15 km, and Ω is increased from 0 to 180 degrees with 10 degree steps. Moreover, the center of the prism is moved within a square of 120×120 km², at 30 km increments, in the east-west and north-south directions with respect to the observed potential anomaly in order to minimize possible errors from any initial visual misplacement of the center. Figure 4 shows the misfit ϵ^2 versus the semimajor axis of the prism for anomaly M7, which is typical among the anomalies. The misfit values are normalized to the minimum misfit value. The selected prism produces a minimum misfit value (see *Arkani-Hamed* [2001b] for examples of observed and modeled anomalies). Figure 5a shows the locations of the centers and the magnetization vectors of the model prisms. The arrows show the horizontal components, and the numbers on the arrows denote the vertical components in A/m. Anomalies M2 and M4 are associated with pairs of nearby bodies with an almost 180 degree difference in magnetization directions. Such is also the case for anomalies M9 and M10, indicating a possibility that the core field had reversed its polarity in between the times these bodies were magnetized.

3.2. Paleomagnetic Pole Positions

[12] The locations of the paleomagnetic poles (Figure 5b) are determined assuming that an individual prism is magnetized in a dipole core field, which is a standard practice in paleomagnetic studies of terrestrial sources [*Butler*, 1992]. N denotes the north pole, and S denotes the south pole. Note that the magnetic lines of the dipole core field are outward in the north pole and inward in the south pole (opposite to the direction of the dipole component of the present Earth's core field). The poles are significantly clustered, 7 out of 10 poles are within a circle of 30 degrees radius centered at about (50°E, 25°S), with their antipoles clustered around (230°E, 25°N). Although the selection criteria, that the anomalies should be small, well-isolated, and simple shaped, did not allow sampling uniformly distributed anomalies over the entire globe, the anomalies still span a great portion of the longitude and latitude. This indicates that the clustering is meaningful and is not dominated by localized sampling. The existence of north and south poles in a given cluster strongly indicates the core field polarity reversals. The pole position of anomaly 3 is in good agreement with that determined by *Hood and Zakharian* [2001], as seen in Figure 5b. I make no attempt to model the magnetic anomaly that is very close to the north pole and was modeled by Hood and Zakharian. This is because the magnetization direction to be determined is sensitive to the details of the magnetic anomaly and no data are available from the part of the anomaly over the

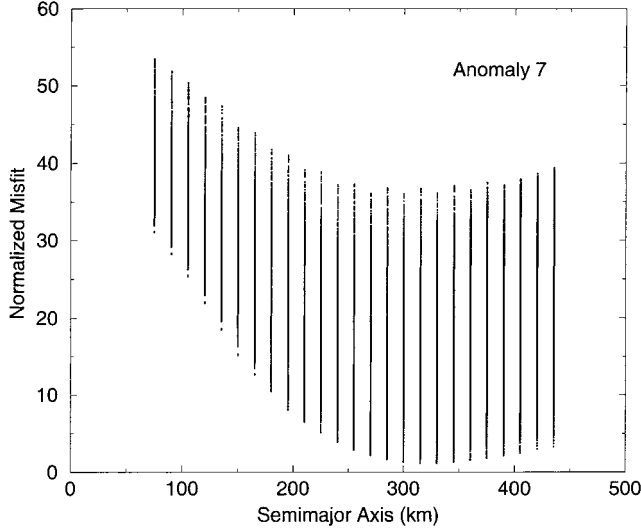


Figure 4. The misfit of model to anomaly 6 versus the semimajor axis (a) of the elliptical prism. Each dot represents a model. The dots overlap and produce the vertical lines.

north pole. The pole positions seen in Figure 5b are also in good agreement with the magnetization vectors of the source models of two smaller magnetic anomalies near Hellas basin which have stronger vertical components compared to their horizontal ones [Arkani-Hamed, 2001a]. The cluster also partly overlaps the much broader region suggested for the paleomagnetic pole locations by Sprenke and Baker [2000] on the basis of the four magnetic profiles investigated by Connerney *et al.* [1999].

4. Magnetization of the Crust

[13] The pole positions determined in the previous section are used to calculate the magnetization of the Martian crust. Using these pole positions eliminates the above mentioned extra non-uniqueness. In the following I first briefly outline the theory and then present the resulting magnetization map of the crust.

4.1. Theory

[14] We note that magnetic anomalies arise from the lateral variations of the magnetization within the magnetic part of Mars, referred to as the magnetic layer in this section. Let $\mathbf{m}(\mathbf{r}_o)$ denote the magnetization at point \mathbf{r}_o inside this layer and $V(\mathbf{r})$ be the magnetic potential at the observation point \mathbf{r} , where $|\mathbf{r}| > |\mathbf{r}_o|$. Then

$$V(\mathbf{r}) = \int \int \int \mathbf{m}(\mathbf{r}_o) \cdot \nabla_o \frac{1}{|\mathbf{r} - \mathbf{r}_o|} r_o^2 \sin \theta_o dr_o d\theta_o d\phi_o, \quad (8)$$

where r_o , θ_o , and ϕ_o are the spherical coordinates at \mathbf{r}_o and the integration is over the entire magnetic layer. Assume that the source bodies have been magnetized by a dipole core field with the axis along the z axis of the coordinate system

$$\mathbf{m}(\mathbf{r}_o) = m\vec{\mathbf{F}} = \left(\frac{m}{\Gamma}\right) \left[(2\cos \theta_o) \vec{\mathbf{r}}_o + (\sin \theta_o) \vec{\theta}_o \right];$$

$$\Gamma = (1 + 3\cos^2 \theta_o)^{1/2}, \quad (9)$$

where $\vec{\mathbf{F}}$ is the unit vector along the dipole core field and $\vec{\mathbf{r}}_o$ and $\vec{\theta}_o$ are the unit vectors in the \mathbf{r}_o and θ_o directions. Bearing in mind that at a given θ_o and ϕ_o the direction of the core field does not significantly change from the top to the bottom of the magnetic

layer and that the magnetic anomaly analysis provides information about the lateral variations of the vertically integrated magnetization, we seek a vertically averaged magnetization and assume that m is not depth dependent. Let $M = m/\Gamma$ and expand it in terms of the spherical harmonics,

$$M(\theta_o, \phi_o) = \sum_{k=1}^N \sum_{l=0}^k [C_{kl} \cos(l\phi_o) + S_{kl} \sin(l\phi_o)] P_{kl}(\cos \theta_o), \quad (10)$$

where C_{kl} and S_{kl} are the expansion coefficients, $P_{kl}(\cos \theta_o)$ is the Schmidt normalized associated Legendre function of degree k and order l , and N is the highest degree considered. Putting (9) and (10) into (8) and after some manipulations (see Arkani-Hamed and Dymant [1996] for details) yields

$$V(r, \theta, \phi) = \sum_{k=1}^N \lambda_{kl} \sum_{l=0}^k [(\alpha_{kl} C_{k+1,l} + \beta_{kl} C_{k-1,l}) \cos(l\phi) + (\alpha_{kl} S_{k+1,l} + \beta_{kl} S_{k-1,l}) \sin(l\phi)] P_{kl}(\cos \theta), \quad (11)$$

where

$$\lambda_{kl} = \frac{a^{k+2} - (a-D)^{k+2}}{r^{k+1}}; \quad \alpha_{kl} = \frac{12\pi k [(k+1)^2 - l^2]^{1/2}}{(k+2)(2k+1)(2k+3)};$$

$$\beta_{kl} = \frac{4\pi(k-1)(k^2 - l^2)^{1/2}}{(k+2)(2k+1)(2k-1)}. \quad (12)$$

Here a (3390 km) is the mean radius of Mars, and D denotes the magnetic layer thickness. Now, the degree 50 model potential $V^o(r, \theta, \phi)$ is expressed as

$$V^o(r, \theta, \phi) = \sum_{k=1}^{50} \frac{a^{k+2}}{r^{k+1}} \sum_{l=0}^k [g_{kl} \cos(l\phi) + h_{kl} \sin(l\phi)] P_{kl}(\cos \theta). \quad (13)$$

Equating (11) and (13) yields

$$g_{kl} = \eta_{kl} C_{k-1,l} + \xi_{kl} C_{k+1,l}, \quad (14)$$

and

$$h_{kl} = \eta_{kl} S_{k-1,l} + \xi_{kl} S_{k+1,l}, \quad (15)$$

where

$$\eta_{kl} = \left[1 - (1 - D/a)^{k+2} \right] \beta_{kl} \quad (16)$$

and

$$\xi_{kl} = \left[1 - (1 - D/a)^{k+2} \right] \alpha_{kl}. \quad (17)$$

Equations (14) and (15) define the relationship between the spherical harmonic coefficients of M and those of the degree 50 model potential.

4.2. Crustal Magnetization

[15] To simplify the mathematical formulation, the dipole axis of the core field is assumed along the z axis of the spherical coordinate system in the above formulation. This is not actually the case as seen in Figure 5. In practice, and for a given paleomagnetic pole position, the degree 50 model potential map is first rotated such that the paleomagnetic pole becomes the north pole of the

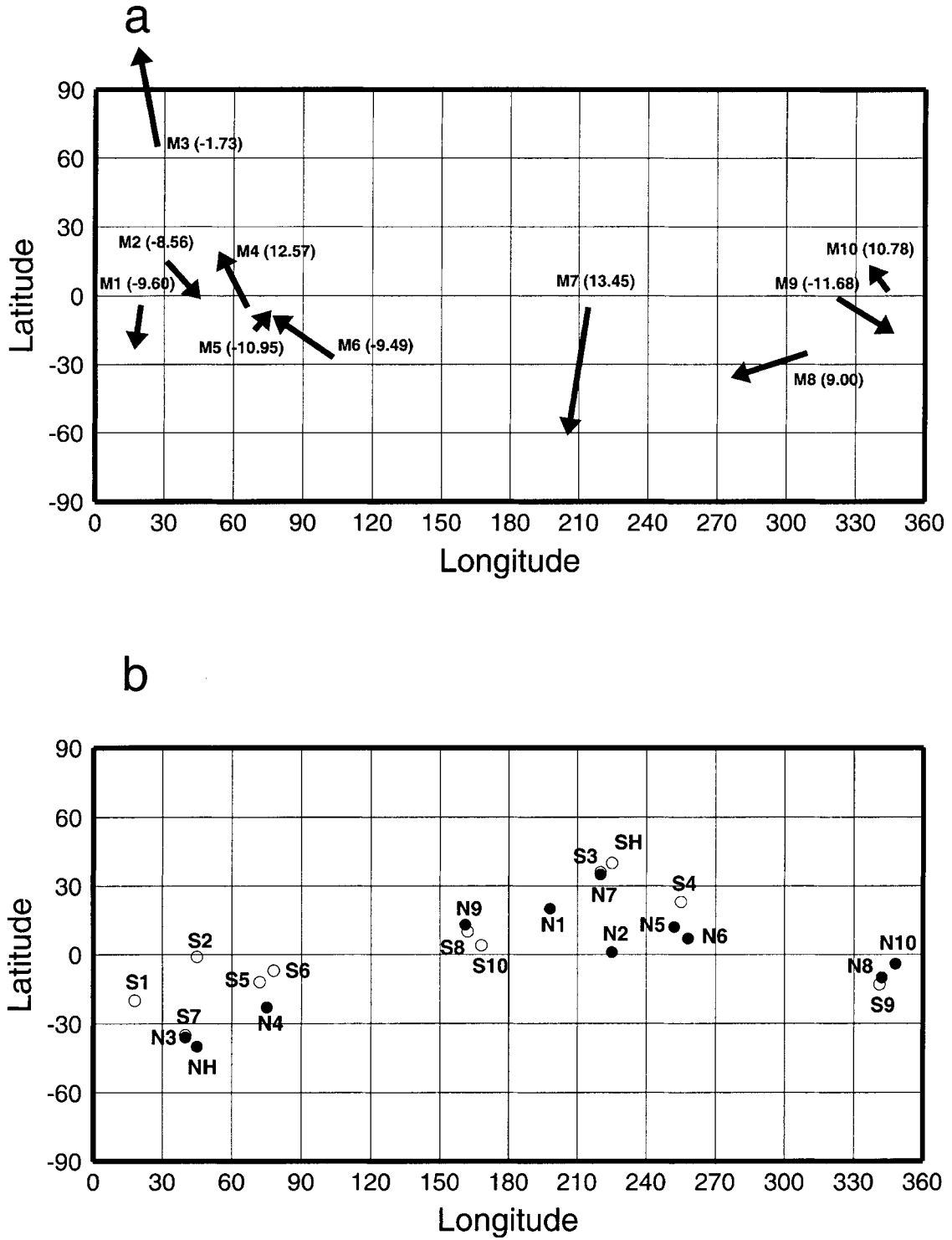


Figure 5. (top) The magnetization vectors of the model prisms. The numbers denote the vertical components of the magnetization (in A/m). (bottom) The paleomagnetic pole positions of the model prisms. N denotes the north pole of the core field, and S denotes the south pole. SH and NH are the south and north poles determined by Hood and Zakharian [2001] for the southern magnetic anomaly near the north pole.

spherical coordinate system. The rotated map is then expanded in terms of the spherical harmonics, and using these new harmonic coefficients, the harmonic coefficients of M are determined from (14) and (15). The 2-D map of M is then constructed, and it is multiplied by Γ , and the resulting map is rotated back to its original position. This final rotated map presents the lateral variations of the

magnetization inside the magnetic layer. Five magnetization models are determined using the north pole positions N1, N2, N6, and N7 (see Figure 5b) and a mean north pole position at (25°N, 230°E) for a nominal magnetic layer thickness of 50 km (see below). The first four pole positions are the extreme positions within the above mentioned paleomagnetic pole cluster. Note that

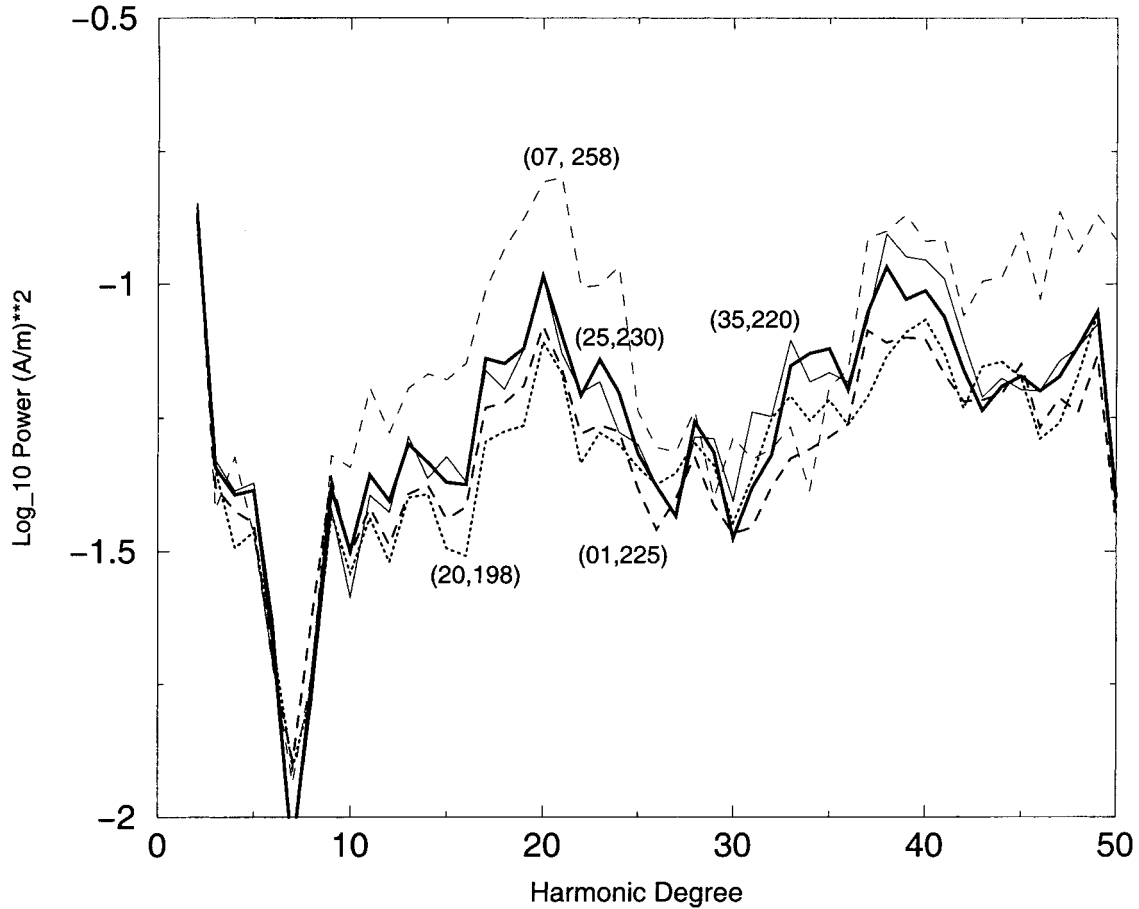


Figure 6. Degree variance of the magnetization models determined using five pole positions. The numbers on the curves denote the latitudes and longitudes of the poles. The thick curve is for the mean pole position.

the unknown core field polarity has no effect on the calculated magnetization. A body that is positively magnetized in a core field with its north pole at the north must be negatively magnetized in a core field with its north pole at the south in order to give rise to the same magnetic anomaly. The magnetization models are very similar, except for that corresponding to N6, as is evident from their degree variance (Figure 6) determined by

$$E_k = \sum_{l=0}^k \left[(m_{kl}^e)^2 + (m_{kl}^o)^2 \right], \quad (18)$$

where m_{kl}^e and m_{kl}^o are the spherical harmonic coefficients of m .

[16] Figure 7 shows the radial and horizontal components of the vertically averaged magnetization of the magnetic layer model derived using the mean pole position. We emphasize that the crustal magnetization is determined under the assumption that the core field pole position remained unchanged (apart from possible polar reversals) during the magnetization of the source bodies. The assumption seems viable if the bodies were magnetized prior to the formation of lateral mass heterogeneities associated with Tharsis bulge, shield volcanoes, and giant impact basins. We also note that owing to the inherent non-uniqueness the magnetization components seen in the figure are not unique. The inverse problem in potential field theory has a fundamental nonuniqueness. Knowing the field (either potential or the three components of the field) everywhere outside a body does not uniquely determine the body. This arises from the very

nature of the potential field, as expressed by (8) for the magnetic potential. Any magnetization, say, $\mathbf{m}^*(\mathbf{r}_o)$, that makes the integral in the right-hand side of this equation vanish can be added to a given solution $\mathbf{m}(\mathbf{r}_o)$. A simple example of such magnetization arises when a spherical shell of constant thickness and uniformly distributed magnetic minerals is magnetized by an internal field [e.g., *Runcorn*, 1975; *Arkani-Hamed and Dymant*, 1996]. This kind of magnetization, that has a varying direction corresponding to the direction of the internal field, can be added to Figure 7. However, such a magnetization has minor effects on the magnetization contrasts (peak-to-trough) seen in Figure 7 since the internal fields of terrestrial planets are usually dominated by the dipole component ($\sim 20,000$ km wavelength in case of Mars). Even if the core field of Mars had considerable quadrupole components, their wavelengths (10,000 km) were much longer than the dominant wavelength (~ 2000 km) of the features seen in Figure 7.

[17] The horizontal magnetization is stronger than the radial one owing to the fact that Terra Cimmeria and Terra Sirenum are located almost in the equatorial zone of the dipole core field, where the core field is almost horizontal. Also, for the same reason, the magnetic potential anomalies (Figure 1) are displaced relative to the source bodies by ~ 200 – 300 km (Figure 7). This is similar to the well-known equatorward displacement of the terrestrial magnetic anomalies relative to their source bodies. We note that using an array of radial dipoles at the surface of Mars as an equivalent source for reducing the radial component of the magnetic field to a fixed altitude by *Purucker et al.* [2000] is

permissible. However, modeling the radial component map by radially magnetized sources [Raymond and Smrekar, 2001] can be misleading. A major part of the radial component of the magnetic field is due to horizontal magnetization as seen from Figures 2a and 7. Moreover, the resulting source body will be directly beneath the magnetic anomaly and does not show the equatorward displacement. We also note that any uncertainty in the paleomagnetic pole position will translate to some uncertainty in the magnetization intensity, by not more than a factor of 2. This is because a magnetic body is always within 90 degrees of the pole of the dipole core field, with two extreme locations: one at the pole, where it is magnetized vertically, and the other at the equator, where it is magnetized horizontally. It requires about two times more horizontal magnetization than vertical magnetization to give rise to a comparable magnetic field outside.

[18] The Martian magnetic sources have retained a strong remanent magnetization acquired in the early history of the planet that is presently comparable in magnitude with the remanent magnetization of fresh extrusive basalt near the oceanic ridge axes of Earth. Bearing in mind the possible reduction of the remanent magnetization through viscous decay and chemical alterations during this very long geologic time (the magnetization of the oceanic basalt decreases by a factor of 4–5 during the first ~20 Myr, largely by chemical alterations [e.g., Bleil and Petersen, 1983]), the initial magnetization of the Martian source bodies must have been even stronger.

5. Discussion and Conclusions

[19] In modeling the magnetization of the 10 small magnetic source bodies, I use the potential maps extracted from the degree 50 model, rather than the raw data along the satellite tracks. This is because the raw data contain contributions from external fields arising from ionospheric and magnetospheric currents which are normally time varying owing to temporal variations of solar wind. A short-period time-varying external magnetic field detected by a moving satellite resembles a spatially varying magnetic field of the crust. These two fields cannot be separated without using a reliable external field model, which is not yet available. On the other hand, in the process of developing a magnetic map, not only the raw data acquired at different times were averaged over bins of 1×1 degree and 10 km height [see Acuna *et al.*, 1999], but also data acquired at different altitude bands and times were used. These processes suppress the time-varying component of the external field owing to its almost random variations. This is probably the reason why the external field components do not produce appreciable differences between the high-altitude and upward continued maps shown in Figure 2. The precesses, however, do not significantly affect the possible quasi-steady component of the external field.

[20] The nominal thickness of 50 km assumed for the magnetic layer of Mars is probably reasonable. Estimates of the mantle temperature of Mars in the first 500 million years of its history [see Schubert *et al.*, 1992, Figure 3], during which the magnetic sources were most likely magnetized, indicate that the depth to the Curie temperature of magnetite (580°C), a mineral that acquires a strong remanent magnetization at high temperatures, did not exceed 50 km. Rock magnetic measurements suggest that the Moho under the Earth's continents is also a magnetic boundary that separates the magnetic crust from the nonmagnetic mantle [Wasilewski *et al.*, 1979]; such may also be the case for Mars. Using chemical analysis of the SNC meteorites and the moment of inertia factor of 0.366 that was determined from Mars Pathfinder data by Folkner *et al.* [1997], Bertka and Fei [1998a, 1998b] proposed chemical models for Mars with a 50 km thick crust. Analysis of the topography and gravity anomalies of Mars led Zuber *et al.* [2000] to suggest an average crustal thickness of 50 km, and Nimmo and Stevenson [2000] set an upper limit of 60 km thick crust on the

basis of the viscous relaxation model of the topography. We note that the thickness of the Martian magnetic layer at around 4 Gyr ago was likely less than the crustal thickness. The upper parts of the Martian crust are probably weakly magnetic because of the lack of magnetic signatures associated with small craters of ~100 km diameter. The impacts that created these craters have most likely increased the temperature of the impact sites by several hundred degrees down to a few kilometers, which could have demagnetized the upper parts of the crust if it had been magnetic to start with. Such a demagnetization could have produced a detectable magnetic anomaly arising from the edge effects if the surrounding crust were magnetic. Furthermore, there is no magnetic signature associated with the north-south topographic dichotomy of Mars. The crustal thickness of Mars estimated on the basis of Mars Global Surveyor topography and gravity data [Zuber *et al.*, 2000] shows a transition zone between the thinner northern crust and the thicker southern crust. However, the zone does not correlate with the topographic dichotomy everywhere, implying that the dichotomy is more surficial and not a fundamental feature of Mars' interior structure [Zuber *et al.*, 2000]. Such a surficial crustal dichotomy must create magnetic anomalies if the upper crust is significantly magnetic. An upper limit of ~2 A/m is estimated for the magnetization of the upper crust on the basis of modeling the magnetic signature of Hellas basin [Arkani-Hamed, 2001a]. This evidence indicates that the Martian magnetic sources are most likely in the lower parts of the crust.

[21] The actual thickness of the magnetic part of the Martian crust D' is most likely different from that of the nominal layer D . Equations (11) and (12) yield the following relationship between the spherical harmonic coefficients of the lateral variations of the vertically averaged actual magnetization m'_{kl} and that of the nominal model m_{kl} , specified by the spherical harmonics of degree k :

$$m'_{kl} = \left[\frac{1 - (1 - D/a)^{k+2}}{1 - (1 - D'/a)^{k+2}} \right] m_{kl}. \quad (19)$$

Roughly speaking, magnetization times thickness does not vary considerably for reasonable thicknesses of the magnetic layer. The magnetizations seen in Figure 7 do not show a distinct seafloor spreading type lineation. The east-west negative trend along 55°S and between 120°E and 210°E in Figure 7b arises because of the common magnetization directions of three nearby source bodies (see below). Although these bodies are better delineated in Figure 7b than in Figure 1, the limited resolution of the degree 50 magnetic potential model still results in a somewhat connected feature. The shortest half-wavelength retained in the model (~215 km) is comparable to the distance between these adjacent bodies. Except for the amplitude, a similar east-west elongated magnetic anomaly exists over central Africa on Earth that connects the Bangui anomaly to the Somali anomaly [e.g., Langel and Estes, 1985; Arkani-Hamed and Strangway, 1986; Cohen and Achache, 1990], which becomes less connected upon inverting the magnetic anomalies to magnetic susceptibility contrasts [see Arkani-Hamed and Dymant, 1996, Figure 7a]. Note also that no external field contribution was taken into consideration in deriving the degree 50 model potential, because of being very small. However, the strong correlation between the morphology of the ionopause [Mitchell *et al.*, 2000] and the east-west elongated pattern of the magnetic anomalies over Terra Cimmeria and Terra Sirenum suggests that some external field component, though minor, is likely incorporated in the model potential that may contribute to the east-west trend in Figure 7b. The magnetic field possibly arising from this almost quasi-steady feature of the ionopause cannot be substantially suppressed by the data averaging within individual bins, as mentioned earlier. The lack of distinct seafloor spreading type magnetic lineation, however, does not argue against possible plate

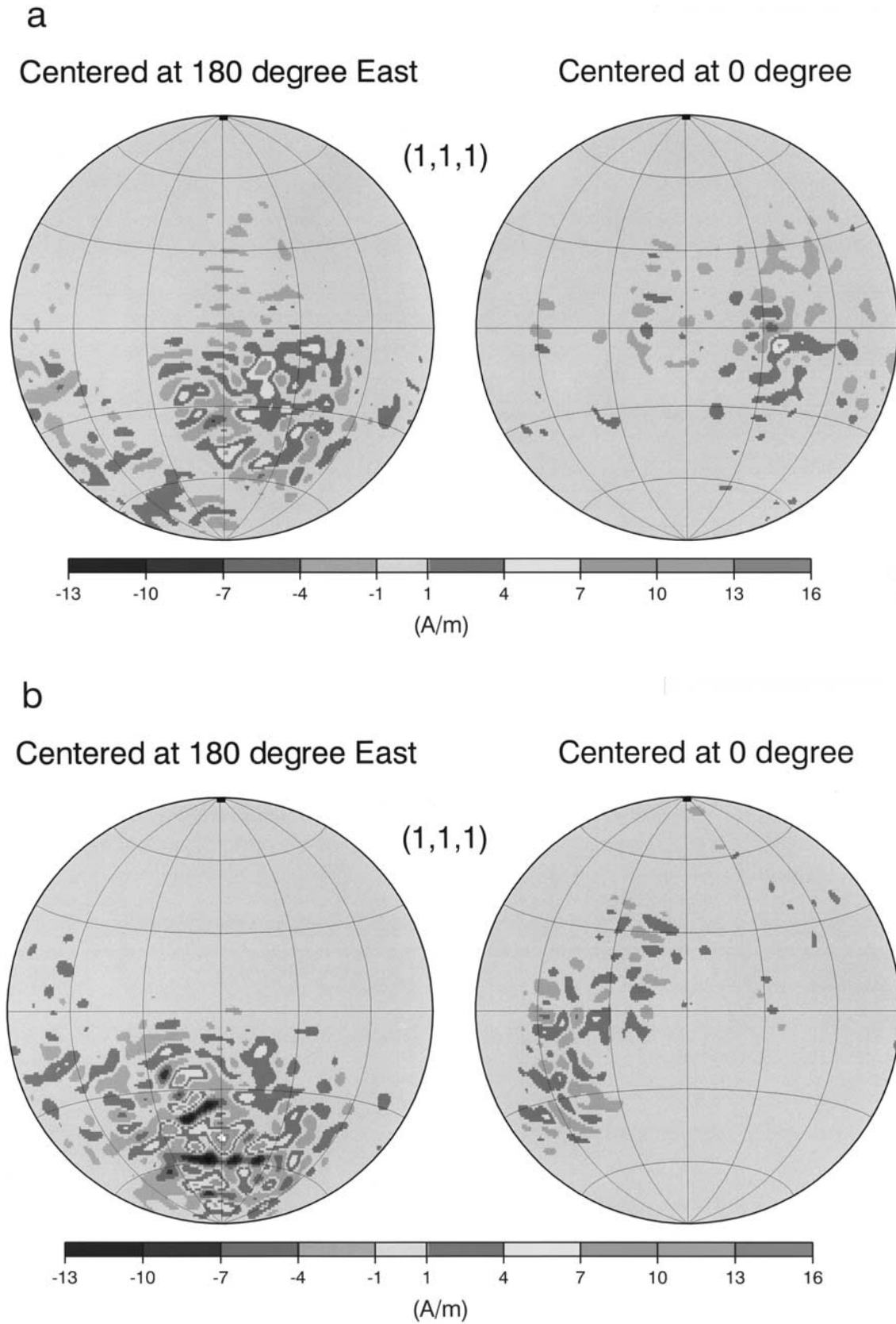


Figure 7. The (a) radial and (b) horizontal components of the crustal magnetization model from the mean pole position. (1, 1, 1) denotes that all three components of the magnetic field are used with equal weighting for the derivation of the potential model. See color version of this figure at back of this issue.

tectonics on Mars [Sleep, 1994, 2000]; rather, it implies that the magnetic data is not reflecting such tectonics.

[22] The magnetic source bodies are very large, having dimensions of several hundred kilometers and a nominal thickness of 50 km. They are comparable in dimension to the magnetic sources of the satellite magnetic anomalies of the Earth that are likely due to the juxtaposition of crustal blocks with different magnetic properties through the plate tectonic processes [e.g., Frey, 1982]. However, the magnetic sources seen in Figure 7 are about an order of magnitude stronger than those of the Earth's continents estimated by many investigators [e.g., Schetzler and Allenby, 1983; Toft and Arkani-Hamed, 1992; Arkani-Hamed and Dymant, 1996]. The Martian core field intensity was likely comparable to that of the present geomagnetic field [Stevenson, 2001]. The strong magnetization of the source bodies of Mars indicates highly magnetic materials with remanent magnetization comparable in intensity to that of the fresh extrusive basalt near oceanic ridge axes on Earth [e.g., Bleil and Petersen, 1983]. The satellite magnetic anomalies of Earth's continents arise from deep-seated magnetic sources in the lower crust [Arkani-Hamed and Celetti, 1989; Langel and Hinze, 1998], which is probably the case with Mars. However, mechanisms other than simple tectonics are necessary to create such intensive and relatively localized magnetic sources in Mars. The magnetic anomalies of Earth's continents are distributed almost uniformly and on a global scale, and there is no vast area devoid of magnetic anomalies, whereas $\sim 1/3$ of the southern hemisphere and almost the entire northern hemisphere of Mars have no appreciable magnetic anomalies. There is ample evidence that FeO content of the Martian mantle is about twice that of the Earth's [Longhi et al., 1992; Sohl and Spohn, 1997; Sanloup et al., 1999]. Whether this high concentration of FeO translates to a high concentration of magnetic minerals depends on the oxidation state of the Martian mantle and lower parts of the crust.

[23] Interpretation of individual magnetic bodies in Figure 7 is beyond the scope of this paper. In the absence of other constraining geophysical data such as heat flow, I examine two general scenarios.

5.1. A Core Field With No Polarity Reversals

[24] As a first scenario, we consider that the Martian core field did not undergo any polarity reversals. This implies that the source bodies are magnetized along the direction of a steady core field and thus positively magnetized. As mentioned earlier, a uniformly magnetic spherical shell that is magnetized by an internal field produces no magnetic anomaly outside. It is therefore possible to add the magnetization of such a shell to Figure 7, as an annihilator, and obtain nonnegative magnetization values. This would require adding as much as 16 A/m and imply that the crust in the northern lowlands and beneath the giant basins in the southern hemisphere is strongly magnetized along the dipole core field. There is evidence that does not support this scenario, in particular, the lack of magnetic signatures associated with the north-south topographic dichotomy, the large shield volcanoes, and giant impact basins. The large impacts that produced the giant basins have delivered a huge amount of heat to the crust. Estimates from lunar impact heating models by Bratt et al. [1985] imply that the large impacts must have heated the Martian crust well above the magnetic blocking temperatures of magnetic minerals and have thermally demagnetized the entire crust beneath the impact sites. Such a pervasive demagnetization would result in strong magnetic anomalies arising from the highly magnetic surrounding crust, unless the impacts occurred in the presence of the core field and the demagnetized parts subsequently cooled and remagnetized. However, to explain the lack of pronounced magnetic signature of the basins with different diameters (Figure 1), a delicate balance must be made between the existing magnetized surrounding crust and the newly remagnetized material consisting of the remaining crust after the impact excavation and possibly the uplifted part of the mantle. A similar argument can be made for the large shield volcanoes such as Olympus and

Tharsis montes that were formed as a result of extensive intrusives and extrusives capable of demagnetizing an appreciable part of the crust. The ages of the shield volcanoes [Hartmann, 1973; Soderblom et al., 1974; Neukum and Hiller, 1981] imply that they were likely formed in the absence of the core field, in which case strong magnetic anomalies are expected if the surrounding crust were highly magnetized. Finally, there is some evidence that the crust of the northern lowlands is old, possibly as old as that of the southern hemisphere, but it is covered by a thin veneer of material that obliterated impact-related surface morphology [Frey et al., 2001]. The crust beneath the lowlands is ~ 40 – 45 km thinner than that of the southern hemisphere [e.g., Zuber et al., 2000]. This substantial variation of the crustal thickness across the dichotomy should create a detectable magnetic field if the crust is magnetized.

5.2. A Core Field With Polarity Reversals

[25] The paleomagnetic pole positions determined through modeling the 10 small, isolated magnetic anomalies are evidence for core field polarity reversals [Arkani-Hamed, 2001b]. It is therefore more plausible that the strongly magnetized source bodies of opposite signs in Figure 7 have been magnetized in different polarity periods. This scenario avoids the need for a strongly magnetized Martian crust, implying that it is similar to the Earth's. The source bodies may arise from local processes that produced highly magnetic materials in the deeper parts of the crust. Some magnetic sources in Figure 7 are circular, suggestive of an impact-related origin. Although an impact that created a large crater with over 200 km diameter easily increased the temperature above 600°C and thermally demagnetized the entire crust beneath the impact site, the weakly magnetic surrounding crust could not give rise to a pronounced magnetic anomaly. It is, however, possible that impact excavation considerably reduced the pressure, causing appreciable partial melting of the FeO rich upper mantle of Mars and production of highly magnetic materials. The depressurized partial melting already occurs beneath the oceanic ridge axes of the Earth, where partial melting of the upper mantle produces the highly magnetic oceanic basaltic crust. The fast upward migration of melt through partially molten porous mantle of Mars, similar to what likely occurs in the upper mantle beneath the oceanic ridge axes of the Earth [e.g., Turcotte and Phipps Morgan, 1992; Sparks and Parmentier, 1994; Ghods and Arkani-Hamed, 2000], possibly focused the melt and created a highly magnetic basaltic cap atop the uplifted mantle plug directly beneath the impact site. The cap then acquired strong magnetization as it cooled in the presence of a core field. The core field polarity reversals then explain the opposite directions of the magnetization. According to this scenario, the large impacts that created the giant basins, Hellas, Argyre and Isidis, must have occurred when the core field had already ceased. These impacts are likely younger than the magnetic bodies in their surroundings [Arkani-Hamed, 2001a]. Although this impact-related magnetization scenario can explain many almost circular features of Figure 7, it has many shortcomings. Impacts are usually randomly distributed in space and time, at least in the first 500 Myr of the planet's history. The impact-related scenario, however, does not explain the lack of comparable magnetic bodies in $\sim 1/3$ of the heavily cratered southern hemisphere. Moreover, there are many noncircular features that require other explanations. Many continental rifts and aulacogens on Earth have distinct magnetic signatures, and some old rifts are strongly magnetic, possibly because of highly magnetic intrusives [e.g., Arkani-Hamed and Strangway, 1985]. Also, slow spreading oceanic ridges on Earth do not usually produce well-defined lineated seafloor spreading marine magnetic anomalies [Ravilly et al., 1998], which are the main characteristics of the intermediate and fast spreading oceans. This is partly because of the lack of prominent magma chamber beneath slow spreading ridges, which results in a segmented basaltic crust. Further investigation is required to verify whether crustal rifting and possibly

very slow spreading have created the three nearby source bodies trending along 55°S and between 120°E and 210°E in Figure 7b.

[26] It is desirable to use other geophysical data to better constrain the magnetic source bodies. The topographic maps I extracted from the 0.25 × 0.25 degree grid MOLA data (15 km grid intervals) showed no distinct and consistent features associated with the magnetic source bodies. I also tried to identify possible gravity anomalies related to the magnetic source bodies by examining a Poisson type relationship,

$$V = \zeta \vec{F} \bullet \nabla U, \quad (20)$$

between the magnetic potential V and the gravitational potential U of the 10 small, isolated magnetic bodies investigated in section 3. ζ in (20) is the proportionality constant. Using harmonics of degree up to 50 of the 75 degree spherical harmonic model of the gravitational potential of Mars [Yuan *et al.*, 2001], to be comparable with the degree 50 model potential, I derived gravitational potential maps at 15 km grid intervals over these bodies. The magnetic potential maps determined from these gravitational potential maps by (20) showed no distinct resemblance to the observed magnetic anomalies of these bodies.

[27] **Acknowledgments.** This research is supported by the Natural Sciences and Engineering Research Council (NSERC) of Canada, grant OGP0041245. I would like to thank Joseph Cain for the spherical harmonic coefficients of their degree 70 model and Mike Purucker and an anonymous reviewer for their useful comments.

References

- Acuna, M. H., Global distribution of crustal magnetization discovered by the Mars Global Surveyor MAG/ER experiment, *Science*, 284, 790–793, 1999.
- Arkani-Hamed, J., A 50 degree spherical harmonic model of the magnetic field of Mars, *J. Geophys. Res.*, 106, 23,197–23,208, 2001a.
- Arkani-Hamed, J., Paleomagnetic pole positions and pole reversals of Mars, *Geophys. Res. Lett.*, 28(17), 3409–3412, 2001b.
- Arkani-Hamed, J., and G. Celetti, Effects of thermal remanent magnetization on the magnetic anomalies of intrusives, *J. Geophys. Res.*, 94, 7364–7378, 1989.
- Arkani-Hamed, J., and J. Dymant, Magnetic potential and magnetization contrasts of Earth's lithosphere, *J. Geophys. Res.*, 101, 11,401–11,425, 1996.
- Arkani-Hamed, J., and D. W. Strangway, An interpretation of magnetic signatures of aulacogens and cratons in Africa and South America, *Tectonophysics*, 113, 257–269, 1985.
- Arkani-Hamed, J., and D. W. Strangway, Band-limited global scalar magnetic anomaly map of the Earth derived from Magsat data, *J. Geophys. Res.*, 91, 8193–8203, 1986.
- Bertka, C. M., and Y. Fei, Density profiles of an SNC model-Martian interior and the moment-of-inertia factor of Mars, *Earth Planet. Sci. Lett.*, 157, 79–88, 1998a.
- Bertka, C. M., and Y. Fei, Implications of Mars Pathfinder data for the accretion history of the terrestrial planets, *Science*, 281, 1838–1840, 1998b.
- Bleil, U., and N. Petersen, Variations in magnetization intensity and low-temperature titanomagnetite oxidation of ocean floor basalts, *Nature*, 301, 384–388, 1983.
- Bratt, S. R., S. C. Solomon, and J. W. Head, The evolution of impact basins: Cooling, subsidence, and thermal stress, *J. Geophys. Res.*, 90, 12,415–12,433, 1985.
- Butler, R. F., *Paleomagnetism*, Blackwell Sci., Malden, Mass., 1992.
- Cohen, Y., and J. A. Achache, New global vector magnetic anomaly maps derived from Magsat data, *J. Geophys. Res.*, 95, 10,783–10,800, 1990.
- Connerney, J. E. P., *et al.*, Magnetic lineations in the ancient crust of Mars, *Science*, 284, 794–798, 1999.
- Ferguson, B. B., J. C. Cain, and D. Mozzoni, An $n = 70$ internal potential function of the Martian magnetic field, *Eos Trans. AGU*, 81, Fall Meet. Suppl. F776, 2000.
- Folkner, W. M., *et al.*, Interior structure and seasonal mass redistribution of Mars from radio tracking of Mars Pathfinder, *Science*, 278, 1749–1752, 1997.
- Frey, H., Magsat scalar anomaly distribution: The global prospective, *Geophys. Res. Lett.*, 9, 277–280, 1982.
- Frey, H., K. M. Shockey, E. L. Frey, J. H. Roark, and S. E. H. Sakimoto, A very large population of likely buried impact basins in the northern lowlands of Mars revealed by MOLA data, *Lunar Planet. Sci.*, XXXII, abstract 1680, 2001.
- Ghods, A., and J. Arkani-Hamed, Melt migration beneath mid-ocean ridges, *Geophys. J. Int.*, 140, 687–697, 2000.
- Hartmann, W. K., Martian surface and crust: Review and synthesis, *Icarus*, 19, 550–575, 1973.
- Hood, L. L., and A. Zakharian, Mapping and modeling of magnetic anomalies in the northern polar region of Mars, *J. Geophys. Res.*, 106, 14,601–14,619, 2001.
- Langel, R. A., and R. H. Estes, The near-earth magnetic field at 1980 determined from Magsat data, *J. Geophys. Res.*, 90, 2495–2509, 1985.
- Langel, R. A., and W. J. Hinze, *The Magnetic Field of the Earth's Lithosphere: The Satellite Perspective*, 429 pp., Cambridge Univ. Press, New York, 1998.
- Longhi, J., E. Knittle, J. R. Holloway, and H. Wanke, The bulk composition, mineralogy and internal structure of Mars, in *Mars*, edited by H. H. Keiffer *et al.*, pp. 184–208, Univ. of Ariz. Press, Tucson, 1992.
- Mitchell, D. L., *et al.*, The shape of Mars' ionosphere and its response to solar activity and crustal magnetic fields: Observations by the MGS electron reflectometer, *Eos Trans. AGU*, 81, Fall Meet. Suppl. F776, 2000.
- Neukum, G., and K. Hiller, Martian age, *J. Geophys. Res.*, 86, 3097–3121, 1981.
- Nimmo, F., and D. Stevenson, Maximum Martian crustal thickness from viscous relaxation of topography, *Proc. Lunar Planet. Sci. Conf. 31st*, abstract 1224, 2000.
- Purucker, M., *et al.*, An altitude normalized magnetic map of Mars and its interpretation, *Geophys. Res. Lett.*, 27, 2449–2452, 2000.
- Raymond, C. A., and S. E. Smrekar, Constraints on sources of strong crustal magnetization in the southern highlands of Mars, *Lunar Planet. Sci.*, XXXII, abstract 2178, 2001.
- Ravilly, M., J. Dymant, P. Gente, and R. Thibaud, Axial magnetic anomaly amplitude along the Mid-Atlantic Ridge between 20°N and 40°N, *J. Geophys. Res.*, 103, 24,201–24,222, 1998.
- Runcorn, S. K., On the interpretations of lunar magnetism, *Phys. Earth Planet. Inter.*, 10, 327–335, 1975.
- Sanloup, C., A. Jambon, and P. Gillet, A simple chondritic model of Mars, *Phys. Earth Planet. Inter.*, 112, 43–54, 1999.
- Schneitzler, C. C., and R. J. Allenby, Estimation of lower crustal magnetization from satellite derived anomaly field, *Tectonophysics*, 93, 33–45, 1983.
- Schubert, G., S. C. Solomon, D. L. Turcotte, M. J. Drake, and N. H. Sleep, Origin and thermal evolution of Mars, in *Mars*, edited by H. H. Keiffer *et al.*, pp. 147–183, Univ. of Ariz. Press, Tucson, 1992.
- Sleep, N. H., Martian plate tectonics, *J. Geophys. Res.*, 99, 5639–5665, 1994.
- Sleep, N. H., Evolution of the mode of convection within terrestrial planets, *J. Geophys. Res.*, 105, 17,563–17,578, 2000.
- Soderblom, L. A., C. D. Codit, R. A. West, B. M. Herman, and T. J. Kriedler, Martian planet wide crater distribution: Implications for geologic history and surface processes, *Icarus*, 22, 239–263, 1974.
- Sohl, F., and T. Spohn, The interior structure of Mars: Implications from SVC meteorites, *J. Geophys. Res.*, 102, 1613–1635, 1997.
- Sparks, W. D., and E. M. Parmentier, The generation and migration of partial melt beneath oceanic spreading centers, in *Magmatic System*, edited by M. P. Ryan, pp. 55–76, Academic, San Diego, Calif., 1994.
- Sprende, K. F., and L. L. Baker, Magnetization, paleomagnetic poles, and polar wander on Mars, *Icarus*, 147, 26–34, 2000.
- Stevenson, D. J., Mars' core and magnetism, *Nature*, 412, 214–219, 2001.
- Toft, P. B., and J. Arkani-Hamed, Magnetization of the Pacific Ocean lithosphere deduced from Magsat data, *J. Geophys. Res.*, 97, 4387–4406, 1992.
- Turcotte, D. L., and J. Phipps Morgan, The physics of magma migration and mantle flow beneath a mid-ocean ridge, in *Mantle Flow and Melt Generation at Mid-ocean Ridges*, *Geophys. Monogr. Ser.*, vol. 71, edited by J. Phipps Morgan, D. K. Blackman, and J. M. Sinton, pp. 155–182, AGU, Washington, D. C., 1992.
- Wasilewski, P. J., H. H. Thomas, and M. A. Mayhew, The Moho as a magnetic boundary, *Geophys. Res. Lett.*, 6, 541–544, 1979.
- Yuan, D. N., W. L. Sjogren, A. S. Konopliv, and A. B. Kucinskis, Gravity field of Mars: A 75th degree and order model, *J. Geophys. Res.*, 106, 23,377–23,401, 2001.
- Zuber, M. T., Internal structure and early thermal evolution of Mars from Mars Global Surveyor topography and gravity, *Science*, 287, 1788–1793, 2000.

J. Arkani-Hamed, Earth and Planetary Sciences, McGill University, 1186 Whiteoaks Avenue, Mississauga, Ontario, Canada, L5J 3B5. (jafar@eps.mcgill.ca)

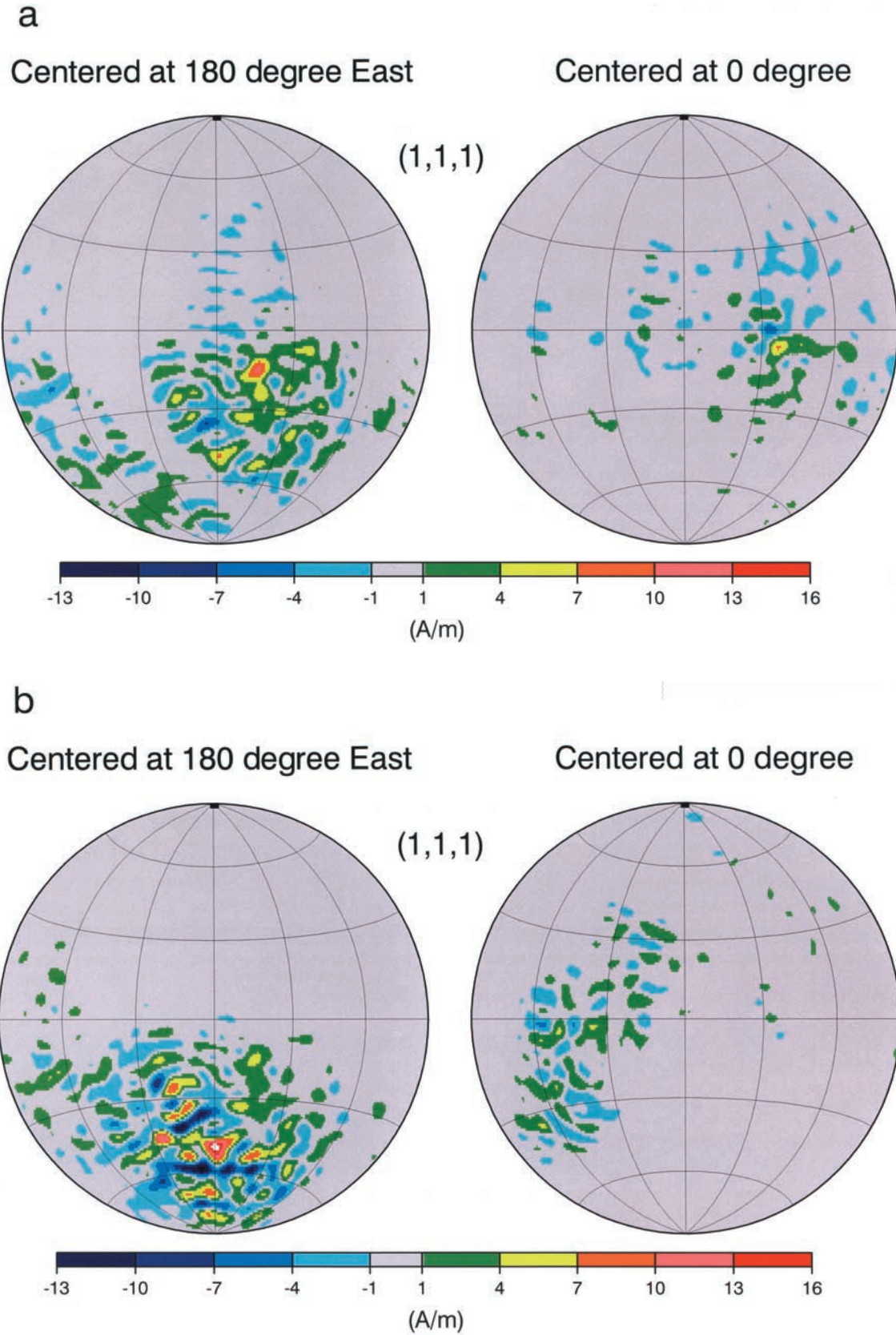


Figure 7. The (a) radial and (b) horizontal components of the crustal magnetization model from the mean pole position. (1, 1, 1) denotes that all three components of the magnetic field are used with equal weighting for the derivation of the potential model.